Operating Point Resolved Loss Calculation Approach in Saturated Induction Machines

Georg Von Pfingsten, Simon Steentjes, and Kay Hameyer, *Senior Member, IEEE*

***Abstract*—In this paper, the global operating point dependent losses of induction machines are studied by using a local transient loss formulation. The level of flux, the machine is operated at, depends on the operation mode of the inverter. Hence, for precise loss modeling of inverter driven induction machines at the machine design stage, the time and spatial distribution of flux density and the influence of choosing the best operating point is included. A loss scaling method is developed to map iron losses calculated at a single synchronous frequency to other frequencies along the torque–speed map. The modeled losses and operating points are compared to extensive machine measurements. By way of example, the effect of different electrical steel grades tailored either to low losses or preferable magnetizability on the machine performance is investigated.**

***Index Terms*—Induction machines (IMs), induction motors, iron loss modeling, loss minimization, loss modeling, magnetic losses, Ohmic losses, ring core measurements, transient finite-element analysis (FEA).**

I. Introduction

INDUCTION machines (IMs) are used as the main workhorse in electrical drive trains due to their low-cost, ruggedness, fault tolerance or particular suitability for certain applications, such as medium- and heavy-duty vehicles. In high power density, machines operating as variable speed drives iron losses have a large share in various operating points due to high magnetic utilization and elaborated field frequencies. On that account, the iron losses need to be considered in all operating points to evaluate the effect of certain design measures or electrical steel grades on the overall performance.

Hence, critical for the selection of the operating point is a loss minimization strategy [1]. The utilized loss model is the linchpin of the predictive accuracy of the loss minimization strategy. Commonly, the machine and loss model parameters are identified from test bench measurements of existing machines [2]–[6]. The variability of the iron losses is represented either by adding a speed-dependent iron loss equivalent resistance to the machine model [6] or by employing variable loss coefficients [7] and elementary iron loss models [8]. All of these approaches solely consider iron losses caused by the fundamental harmonic of the magnetic flux density in the machine, leading to a strong simplification.

For the evaluation of different electrical steel grades or other design measures on the motor efficiency, a loss minimization considering magnetizability and iron loss is indispensable. In [9], a loss minimization is performed at the system level by using a fundamental wave machine model, whereas in [10] saturation is considered through lookup tables. Analytical estimation of squirrel cage induction machine (SCIM) model parameters at the machine design stage is conducted in [10] and [11]. However, in [12] it is shown that for highly utilized traction drives, the study of saturation significantly contributes to IM design.

In this paper, a transient iron loss model in combination with a scaling method to estimate occurring losses at different synchronous frequencies is used to predict the iron losses. This allows studying the global operating point dependent losses of IMs considering the effect of higher harmonics and minor loops efficiently. In [13] and [14], it is shown that the iron losses are underestimated if only the fundamental field-wave is considered. The transient loss formulation is parameterized by standardized measurements on ring cores. Therewith, an *a priori* estimation of loss minimized operating points in IMs is possible avoiding tedious frequency domain simulations and extensive test bench measurements of existing machines. Using this operating point dependent loss determination, the effect of different electrical steel grades tailored either for low losses or for preferable magnetization behavior on the machine performance is studied as an application example.

Applying this method, the global operating point dependent losses of a four-pole ($2p = 4$) SCIM for an electric vehicle traction application are studied through measurements and finite-element (FE) simulations. The machine is driven by a MOSFET inverter with a nominal dc-link voltage of 130 V in the application. The machine can deliver a short-term maximum power of 37 kW and has a maximum operating speed of $n_{\max} = 8000$ r/min. The stator has $N_1 = 36$ slots, which is equal to the number of slots per pole and phase of $q_1 = 3$. The rotor has $N_2 = 28$ bars/slots. The squirrel cage is made up of aluminum in a die casting process.

The paper is structured as follows. First, the simulation of the machines operating points is discussed. Second, the modeling of the operating points from FE simulation is addressed. In the next step, the dynamic iron loss model is described. Subsequently, the scaling of the modeled iron losses from one simulated fundamental frequency to another fundamental frequency is discussed. From the scaling scheme, the iron losses

Manuscript received February 29, 2016; revised May 13, 2016; accepted June 1, 2016. Date of publication August 2, 2016; date of current version February 9, 2017. This work was developed in the context of the cooperative project "MAs:Stab," sponsored by the German Federal Ministry of Economic Affairs and Energy (BMWi) under Grant 01MY12008A.

The authors are with the Institute of Electrical Machines, RWTH Aachen University, 52056 Aachen, Germany (e-mail: georg.vonpfingsten@iem.rwth-aachen.de; simon.steentjes@iem.rwth-aachen.de; kay.hameyer@iem.rwth-aachen.de).

Color versions of one or more of the figures in this paper are available online at http://ieeexplore.ieee.org.

Digital Object Identifier 10.1109/TIE.2016.2597761

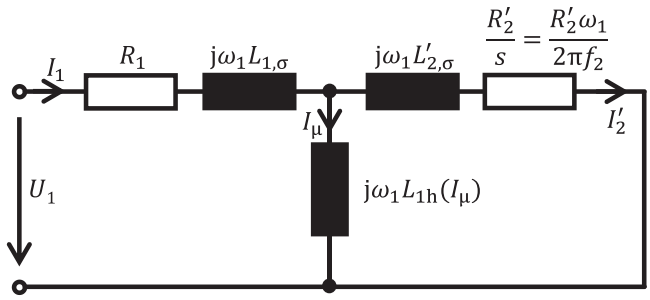

Fig. 1. Fundamental wave T–equivalent-circuit of the SCIM.

are modeled versus the entire torque speed operating map. The modeled operating points of the machine and losses are compared to machine measurements. Finally, the simulation scheme is used to analyze the influence of different electric steel grades on the machine behavior. The paper ends with a discussion of the results and conclusions.

II. Machine Simulation Scheme

Traction drives, such as in automotive application, are operated in a wide range of torque and speed. The entire operating range in terms of torque and speed is of interest. Hence, the losses are given in torque–speed (T–n) operating points.

A. Determination of Torque Speed Operating Points

A nonlinear transient FE formulation with single valued magnetization curves is used to model the local flux density values of the magnetic circuit. The stator current is the only excitation defined in the model. The rotor position and speed n are used to update the rotational boundaries in the air gap in every simulation step. Hence, the stator current (amplitude I_1 and frequency f_1) as well as the slip frequency $f_2 = f_1 - np$ are used to define the operating point in the FE model.

The fundamental wave T–equivalent-circuit (see Fig. 1) illustrates the allocation of the given stator current I_1 into the magnetizing current I_μ and the rotor current I'_2. All reactances and the rotor resistance are proportional to the synchronous angular frequency ω_1. When the voltage drop on the stator resistance R_1 is subtracted, the allocation of the stator current I_1 into the magnetizing current I_μ and the rotor current I'_2 is independent of f_1. Since the saturation of the main inductance has to be considered in highly utilized traction drives, this allocation depends only on f_2 and the saturation of the main inductance L_{1h}.

Therefore, the operating points of the IM can be mapped in the stator current slip frequency plane (I_1–f_2 plane). This mapping of measured machine operating points in terms of torque T and speed n (see Fig. 2) to the I_1–f_2 plane is shown in Fig. 3. The colors of the operating points correspond to their numbering from 1 to 200. Since the same operating points are shown in Figs. 2 and 3, the operating point numbers, i.e., color of the operating point, are associated.

The operating points of the machine can be simulated by spanning an area by a reasonable number of combinations of I_1 and f_2 because the machine operating points are covered on the I_1–f_2 plane.

In the machine measurements, the total harmonic distortion (THD) of the stator current I_1 was measured. In most of the

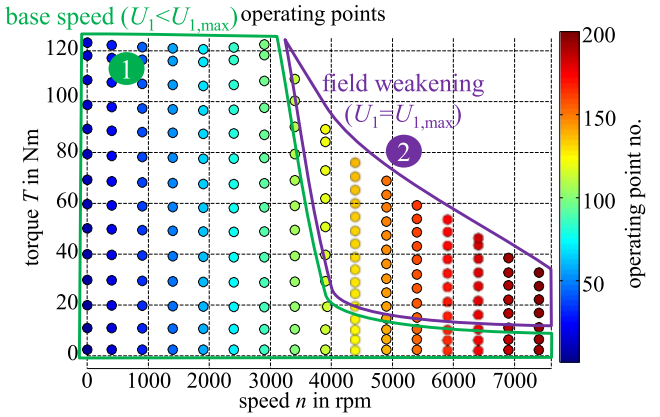

Fig. 2. Measured operating points of the machine in the torque–speed (T–n) plane.

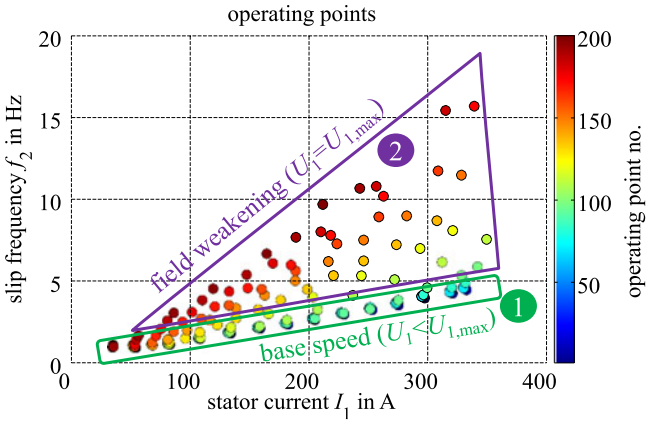

Fig. 3. Measured operating points of the machine in the stator current slip frequency (I_1–f_2) plane.

operating points, the value of the THD is between 1% and 2%. Except for the no-load operating points ($I_1 = 0, T \approx 0$), in all operating points the value of the THD is less than 5%. Therefore, the stator current can be assumed as sinusoidal and the error of neglecting harmonics in the stator currents by inverter switching or from the machines circuit is neglected when modeling the Ohmic losses in the stator.

Nonlinear transient FE simulations of the machine are conducted to model the appropriate operating points in terms of torque and speed. One-hundred combinations of I_1 and f_2 are simulated in order to cover the entire operating range of the machine. A sinusoidal stator current density (and therefore sinusoidal current I_1) is used as excitation for the simulation. Figs. 4 and 5 show the simulation results in terms of torque T and stator flux linkage Ψ_1 in the I_1–f_2 plane. It is apparent that the stator flux linkage Ψ_1 is subject to saturation at high stator currents and low slip frequency.

Fig. 6 shows the simulated torque and stator flux linkage as projected views. The current densities in the rotor are calculated in the postprocessing of the FE simulations. Using these current densities and their local distribution over the rotor bars, the Ohmic losses in the rotor are determined. Since the stator current is assumed to be sinusoidal during simulation, the stators Ohmic losses are easily calculated. The sum of the Ohmic

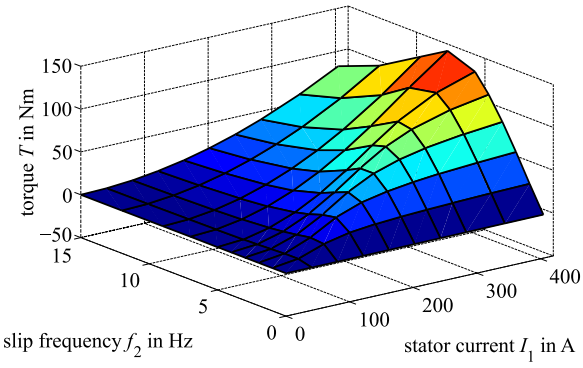

Fig. 4. Simulated torque of the machine (from FE simulations).

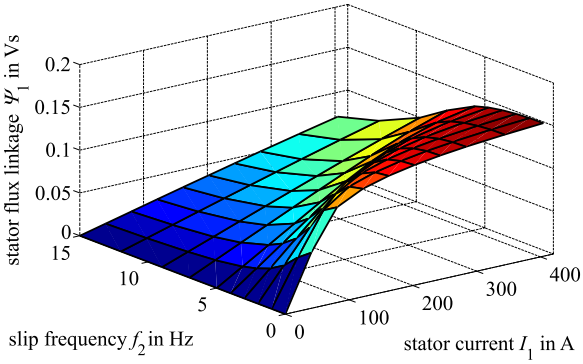

Fig. 5. Simulated stator flux linkage of the machine (from FE simulations).

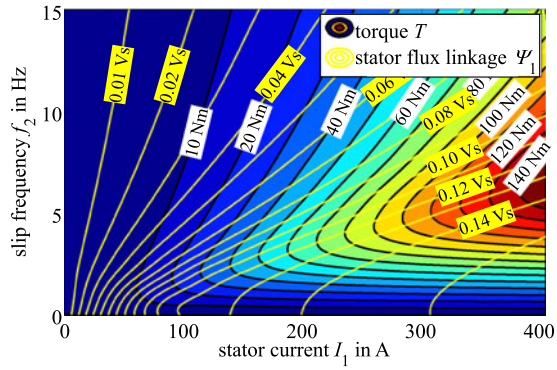

Fig. 6. Simulated torque and stator flux linkage of the machine.

losses P_{Cu} in a stator and a rotor and the torque T is shown in Fig. 7.

The operating points of the machine are determined from the simulation results shown in Figs. 6 and 7. For every desired torque and speed combination, the $(I_1{-}f_2)$ operating point with the highest efficiency (lowest losses) is sought:

$$\begin{aligned} &\min_{I_1,f_2} P_{\mathrm{Cu}}(I_1,f_2) \\ &s.t.\ T(I_1,f_2) = T_{\mathrm{req}} \\ &f_1 = f_2 + n_{\mathrm{req}} \cdot p \\ &U_1(I_1,f_1) \le U_{\max}. \end{aligned} \tag{1}$$

If this $(I_1{-}f_2)$ combination violates the voltage limit of the inverter, an operating point with less stator flux linkage is chosen.

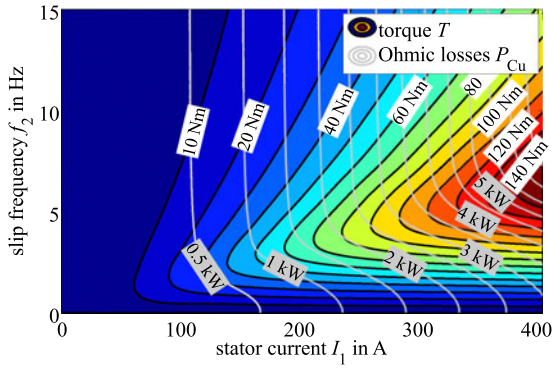

Fig. 7. Simulated torque and Ohmic losses of the machine.

If no point exists, which meets the required torque at the maximum feasible stator flux linkage, the torque–speed combination is found to be not obtainable with the given boundaries.

The resulting simulated operating points are compared to machine measurements in Section II-D.

B. Iron Loss Modeling

The maximum fundamental operating frequency of the stator current is 282 Hz. This high frequency leads to significant influence of flux pulsations in the teeth of the machine up to frequencies of multiple kHz. Since the fundamental frequency of the rotor current f_2 is between 0 and 16 Hz, a wide spread of the magnetizing frequencies in the rotor and stator soft magnetic material is apparent. When using time harmonic formulations to model the iron losses, a minimal period of $T_{\min} = 1/f_2$ has to be simulated. For the minimal considered (except for $f_2 = 0$) slip frequency of 1 Hz, this leads to a simulation time of $T_{\min} = 1$ s to cover one full magnetization period in the rotor. To prevent subsampling and aliasing of the magnetic flux pulsations in the teeth from slotting harmonics, a sampling frequency of several thousand Hz is necessary. In combination with the simulation time period of $T_{\min} = 1$ s, this would lead to multiple thousand time steps per simulation and thus to an inadequately high computational effort.

To avoid the disadvantage of high computational effort, it is advantageously to shift from time-harmonic iron loss models to those formulated in the time domain [12]–[20]. In this paper, a transient formulation of the iron loss calculation (2)–(5) in the machine is utilized [14], [15]. The instantaneous hysteresis loss $p_{\mathrm{hy}}(t)$ is given in W/kg and is described by the time differential of the local flux density in the radial (B_{r}) and tangential (B_{ϑ}) directions, the irreversible magnetic field strength H_{irr}, and the specific density of the material ρ, as shown by

$$p_{\mathrm{hy}}(t) = \rho \cdot \left\{ \left| H_{\mathrm{irr}} \frac{\mathrm{d}B_{\mathrm{r}}}{\mathrm{d}t} \right| + \left| H_{\mathrm{irr}} \frac{\mathrm{d}B_{\vartheta}}{\mathrm{d}t} \right| \right\}. \tag{2}$$

The Foucault (macroscopic) eddy-current loss $p_{\mathrm{cl}}(t)$ is described as the time derivative of the magnetic flux density and the material-dependent iron loss parameter k_{cl}

$$p_{\mathrm{cl}}(t) = k_{\mathrm{cl}} \cdot \frac{1}{2\pi^2} \cdot \left\{ \left| \frac{\mathrm{d}B_{\mathrm{r}}}{\mathrm{d}t} \right|^2 + \left| \frac{\mathrm{d}B_{\vartheta}}{\mathrm{d}t} \right|^2 \right\}. \tag{3}$$

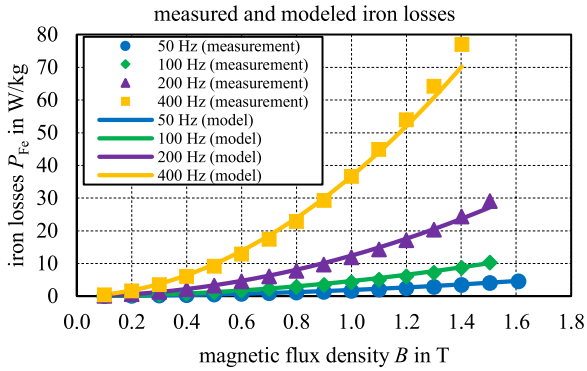

Fig. 8. Measured (ring core) and modeled iron losses for sinusoidal flux density waveform for the material M400-50A.

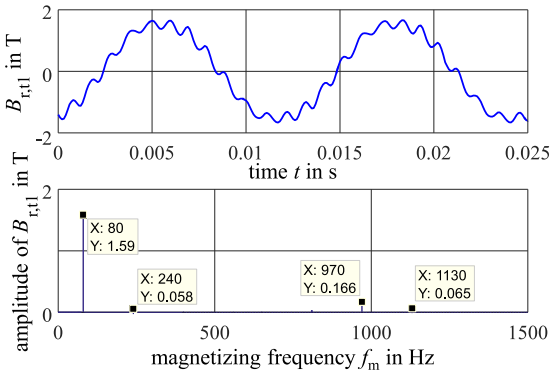

Fig. 9. Simulated flux density in the center of the stator teeth at $f_1 = 80$ Hz.

TABLE I
IDENTIFIED IRON LOSS PARAMETERS

Parameter	M400-50A	M250-50A	M330-35AP	M470-50HP	Unit
k_{hy}	25.9	11.2	20.9	23.4	$10^{-3}\cdot$ W·kg^{-1}·s·T^{-2}
k_{cl}	125.7	91.7	62.7	178.0	$10^{-6}\cdot$ W·kg^{-1}·s^{2}·T^{-2}
k_{ex}	779	828	584	862	$10^{-6}\cdot$ W·kg^{-1}·s$^{1.5}$·T$^{-1.5}$

The excess (microscopic) eddy current losses $p_{ex}(t)$ are evaluated using the material-dependent loss parameter k_{ex} as

$$p_{ex}(t) = k_{ex} \cdot \frac{1}{8.763} \cdot \left\{ \left| \frac{dB_r}{dt} \right|^2 + \left| \frac{dB_\vartheta}{dt} \right|^2 \right\}^{0.75}. \quad (4)$$

The sum of the three iron loss components, i.e., the total iron losses $p_{Fe}(t)$, is calculated according to

$$p_{Fe}(t) = p_{hy}(t) + p_{cl}(t) + p_{ex}(t). \quad (5)$$

In [14] and [15], the static hysteresis loop is approximated by an equivalent ellipse. From the ellipse formulation, H_{irr} is modeled by the maximum absolute flux density that is reached in the history of the material B_{max}, the actual absolute value of the flux density B, and the hysteresis loss parameter k_{hy}, as shown by

$$H_{irr}(B, B_{max}) = \frac{k_{hy} \cdot B_{max}}{\pi \cdot \rho} \cdot \cos\left(\text{asin}\left(\frac{B}{B_{max}}\right)\right). \quad (6)$$

The iron loss parameter k_{cl} is calculated using the material constants, sheet thickness d, specific electrical resistivity ρ_e, and ρ as given in [21]

$$k_{cl} = \frac{\pi^2 d^2}{6 \cdot \rho \cdot \rho_e}. \quad (7)$$

In order to find the values of the loss parameters k_{ex} and k_{hy}, ring core measurements of the soft magnetic material are conducted with sinusoidal flux density waveform. Fig. 8 shows the comparison of the measured and modeled iron losses for the steel grade M400-50A. The identified iron loss parameters are given in Table I.

C. Scaling Iron Losses According to Different Synchronous Frequencies f_1

Due to the fact that the FE simulations are performed for a single synchronous frequency f_1, a suitable scaling algorithm for the iron losses at different synchronous frequencies has to be applied. From the simulated locally distributed and temporal-dependent magnetic flux density in the core material, the iron losses are studied. For example, the operating point at $I_1 = 202$ A and $f_2 = 5$ Hz is studied at $f_1 = 80$ Hz and $f_1 = 240$ Hz. Fig. 9 shows the magnetic flux density in the center of a stator tooth in the radial direction $B_{r,t1}$ over time and as a frequency spectrum for $f_1 = 80$ Hz. The relevant frequency components for the iron losses are identified as 80, 870, and 1130 Hz. From the frequency spectra in all FE elements in the rotor and stator iron, the local iron losses are calculated and summed up to get the total iron losses. From the frequency-dependent iron losses, the cumulated iron losses are calculated. The following equation gives this formulation for the stator Foucault eddy current losses $p_{cl,1,sum}$:

$$p_{cl,1,sum}(f_k) = \sum_{m=1}^{k} p_{cl,1}(f_m) \quad (8)$$

with k being the order of the minimum simulated magnetizing frequency $f_{min} = T_{sim}^{-1}$, the simulated time T_{sim}, and the maximum considered frequency f_k. The maximum considered frequency is described by $f_k = k \cdot f_{min}$.

Fig. 10 ($f_1 = 80$ Hz) and Fig. 11 ($f_1 = 240$ Hz) show the cumulated stator Foucault eddy current losses $p_{cl,1,sum}$ as defined in (8) as a function of the upper frequency boundary f_k.

The Foucault stator iron losses that occur at base frequency are 9.2 W ($f_1 = 80$ Hz) and 83.1 W ($f_1 = 240$ Hz). This equals to a factor of 9, which is equal to the square of the increase in frequency f_1 (factor of 3). The mechanical frequency in this example is $n = 37.5$ 1/s and $n = 117.5$ 1/s correspondingly. This leads to flux pulsations in the stator teeth at the frequencies $f_{fp,1} = 970$ Hz and $f_{fp,1} = 1030$ Hz ($f_1 = 80$ Hz, $f_2 = 5$ Hz) and $f_{fp,1} = 3050$ Hz and $f_{fp,1} = 3530$ Hz ($f_1 = 240$ Hz, $f_2 = 5$ Hz). The dependencies of the flux pulsating frequencies in the stator $f_{fp,1}$ and in the rotor $f_{fp,2}$ from the mechanical speed n and the slot numbers N_1 and N_2 are given in the

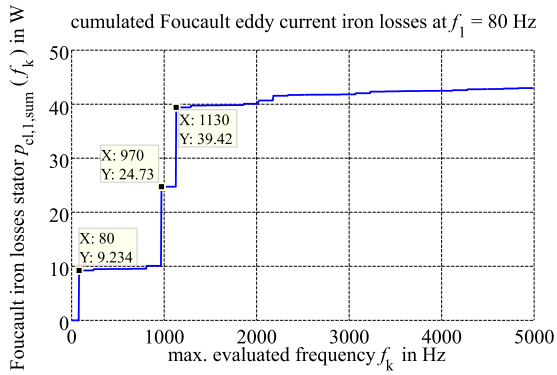

Fig. 10. Simulated cumulated Foucault eddy current iron losses in the frequency domain for the base frequency of $f_1 = 80$ Hz.

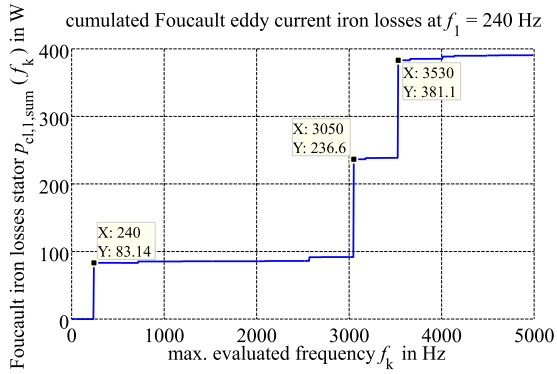

Fig. 11. Simulated cumulated Foucault eddy current iron losses in the frequency domain for the base frequency of $f_1 = 240$ Hz.

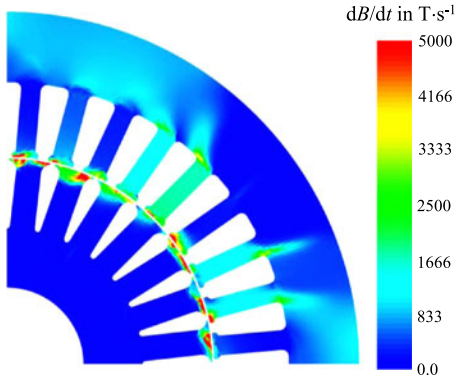

Fig. 12. Simulated time derivative (between two consecutive simulation time steps) of the flux density at $f_1 = 80$ Hz, $f_2 = 5$ Hz, $I_1 = 202$ A.

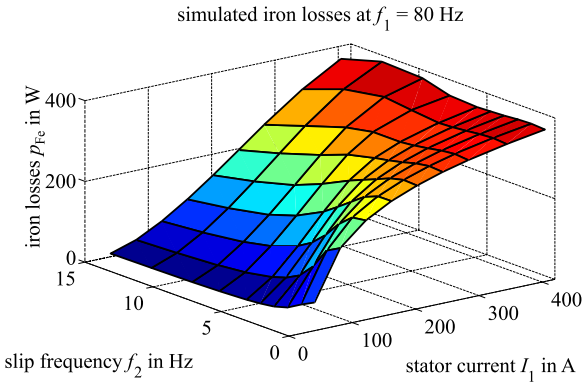

Fig. 13. Simulated iron losses of the machine at a base frequency of 80 Hz (el. steel grade: M400-50A).

following equations:

$$f_{\mathrm{fp},1} = m_1 \cdot n \cdot N_2 \pm f_1, \quad m_1 = 1, 2, \ldots \tag{9}$$

$$f_{\mathrm{fp},2} = m_2 \cdot n \cdot N_1 \pm f_2, \quad m_2 = 1, 2, \ldots. \tag{10}$$

When examining the iron losses in Figs. 10 and 11, it is found that the highest share in the overall iron losses is caused by the flux pulsations at $f_{\mathrm{fp},1}$ (correspondingly for the rotor at $f_{\mathrm{fp},2}$). Since $n \cdot N_1 >> f_2$ and $n \cdot N_2 >> f_1$ can be assumed for most machines, it is assumed that the frequency of the flux pulsations can be scaled according to the speed n. This assumption is underlined by the local distribution of the time derivative of the flux density dB/dt in the machine. Fig. 12 shows the local dB/dt. The highest values of dB/dt > 5000 T $\cdot$ s^{-1} are found at the tips of the stator and rotor teeth. Values of dB/dt > 800 T $\cdot$ s^{-1} are found in the stator teeth and yoke. This local distribution illustrates the fact that the largest share of iron losses is caused by the flux pulsations.

According to this procedure, the iron loss terms (2)–(4) are evaluated in the stator and rotor at one simulation frequency ($f_1 = 80$ Hz) and the loss components are subsequently scaled as

$$p_{\mathrm{hy}} \propto n \tag{11}$$

$$p_{\mathrm{cl}} \propto n^2 \tag{12}$$

$$p_{\mathrm{ex}} \propto n^{1.5}. \tag{13}$$

The smallest error in the sum of all losses while scaling from 80 to 240 Hz of 1.45% is found when scaling the losses according to (11)–(13). The largest relative error of 34.72% (2.59 W) is made when scaling the rotor hysteresis losses. However, since the hysteresis losses in the rotor are small when compared with the other loss components, the absolute error value of 2.59 W is found to be sufficiently precise. The application of these scaling factors (11)–(13) to the simulated iron losses at $f_1 = 80$ Hz (see Fig. 13) leads to the scaled iron losses at $f_1 = 240$ Hz (see Fig. 14).

In the following, this scaling scheme is used to scale the iron losses to the different operating frequencies f_1 of the simulated operating points. Fig. 15 shows the simulated iron losses P_{Fe} in terms of torque and speed when choosing the operating points (I_1, f_2) with the lowest possible losses for the requested torque T and speed n, as described in Section II-A. To take into account the influence of the iron losses on the magnetic circuit, the iron losses are subtracted from the electric generated torque.

D. Comparison of Machine Measurements and Simulations

The machine behavior is highly influenced by the rotor temperature. Therefore, the rotor temperature in the test bench measurements is measured. Since the installation of temperature sensors in the rotor cage requires holes in the rotor cage,

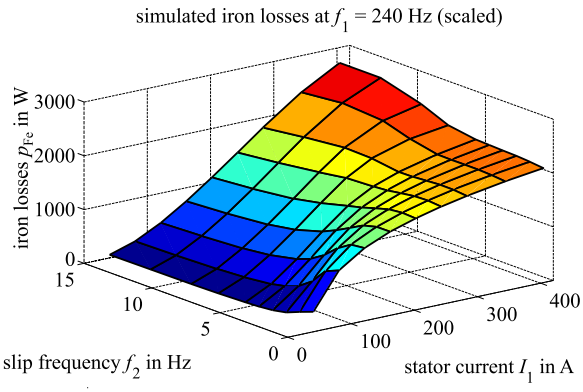

Fig. 14. Scaled simulated iron losses of the machine at a base frequency of 240 Hz (el. steel grade: M400-50A).

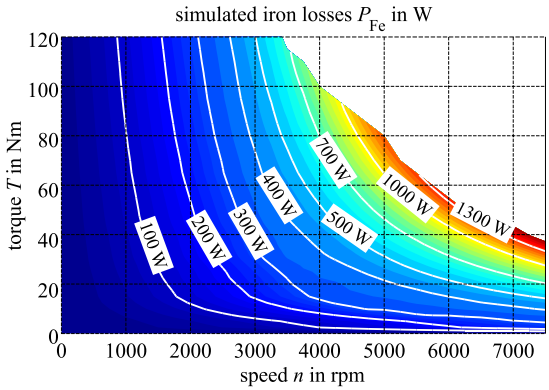

Fig. 15. Simulated machine iron losses (electrical steel grade: M400-50A).

the rotor resistance and therefore the machine behavior is influenced drastically. Hence, we use noncontact infrared (IR)-temperature measurement on the surface of the short circuit ring. Thus, the rotor surface is spray-painted black to create a nonreflecting surface at IR, i.e., an IR-emissivity > 0.97. The IR-temperature measurement of the rotor temperature θ_{rotor} was validated using a second machine equipped with four Pt-100 temperature sensors in the rotor cage and a rotor telemetry system. Seven temperature sensors are used in different positions inside the stator winding to measure the average winding temperature $\theta_{\mathrm{winding}}$. Fig. 16 shows the setup of the test bench. The influence of inverter switching on the losses of the machine is analyzed by adding a low-pass filter to the power analyzer. Through comparing the measured electric input power with and without low-pass filtering input voltages and currents, the influence of inverter switching on the machine losses is accounted for. For the measured machine we measured the influence of switching as less than 20 W. Hence, the losses from switching are not taken into account in the machine simulation.

The operating points from machine measurements (see Fig. 2) are compared to the simulated operating points in terms of torque T and speed n. Figs. 17 and 18 show the stator current I_1 and the slip frequency f_2 from measurement and the proposed simulation scheme. The displayed results show a good match between

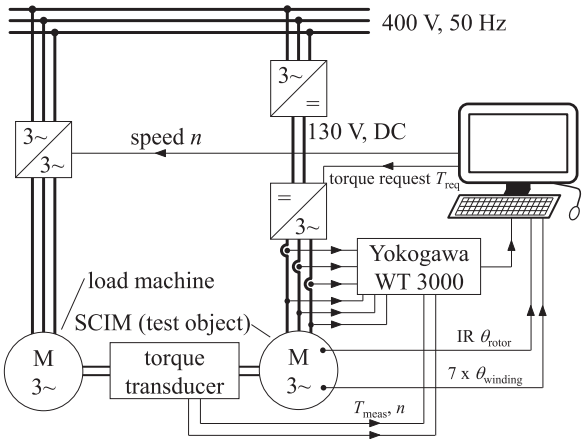

Fig. 16. Test bench setup.

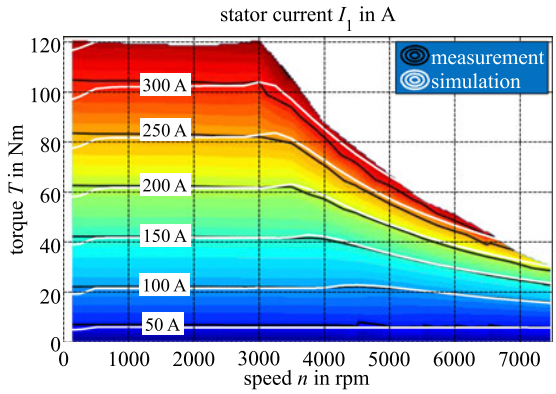

Fig. 17. Comparison of measured (black lines) and simulated (white lines) stator current.

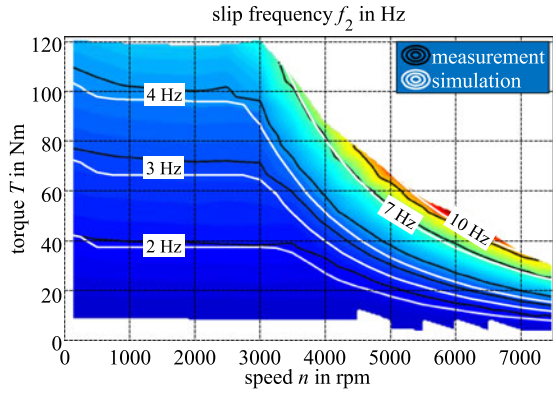

Fig. 18. Comparison of measured (black lines) and simulated (white lines) slip frequency.

simulated and measured operating behavior in terms of the modeling of the T–n operating points.

The Ohmic losses P_{Cu} in the measurement highly depend on the temperature $\theta_{\mathrm{winding}}$ of the stator winding and θ_{rotor} of the rotor cage (14). Since the winding and rotor cage temperature are not constant during the measurement of a torque–speed map, the

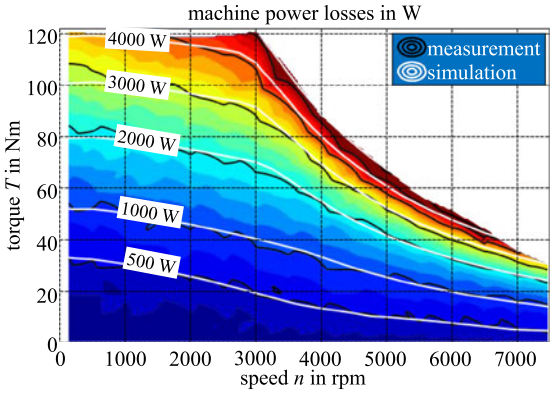

Fig. 19. Comparison of measured (black lines) and simulated (white lines) machine power losses.

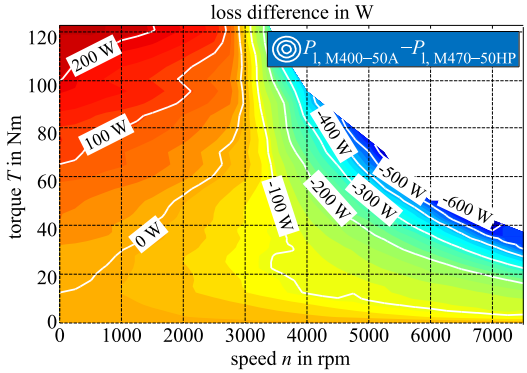

Fig. 20. Simulated difference of the machine power losses when using the two electrical steel grades M400-50A and M470-50HP.

Ohmic losses are corrected regarding the measured temperature in rotor and stator according to

$$P_{\mathrm{Cu}}(\theta) = 3 \cdot \left(1 + \Delta\theta \cdot 3.9 \cdot 10^{-3} \cdot \mathrm{K}^{-1}\right) \cdot R_{\mathrm{ref}} I^2. \quad (14)$$

These corrected losses are compared to the simulated losses in Fig. 19. For the studied machine, the influence of additional ac winding losses was studied according to [22]. At speed $n = 3500$ r/min, the increase of the stator winding losses due to ac excitation is 3.6%. At maximum speed, the maximum increase of 19% was modeled. The cause for this current reduction is the limitation of stator flux linkage Ψ_1 due to the voltage limit. Since higher values of I_1 lead to higher stray flux, Ψ_1 is increased. Hence, the maximum current has to be reduced at high speeds (see Fig. 17). At maximum speed, the maximum current is limited to $I_1 < 200$ A. At base speed, the maximum current is limited to $I_1 < 350$ A. The iron losses increase with frequency. Hence, the influence of the increase of the ac winding losses on the total machine losses is small. Therefore, the ac component of the stator winding losses is not considered in the simulation scheme for the studied machine design.

Fig. 19 shows very good agreement between measured and simulated power losses. Since the loss model starts from local magnetic flux density waveforms and thus inherently incorporates the most important loss dissipating effects (flux pulsations, harmonics in rotor current, rotor current displacement, and iron losses), it can be utilized to model the influence of different design factors of the machine. Besides other design factors, the following ones can be studied using the loss model:

1) electric steel grade;
2) air gap length;
3) number of poles;
4) axial active length;
5) number of turns;
6) number of slots per pole and phase q_1;
7) number of rotor slots N_2; and
8) cage material (copper instead of aluminum).

In the following, we will discuss the influence of the choice of stator's and rotor's electric steel grades based on the losses dissipated in the machine.

III. Simulation of the Influence of Different Electric Steel Grades on the Behavior of the IM

The influence of the electric steel grade on the power losses is analyzed by subtracting the simulated power losses of, respectively, two materials. Hence, not only the difference in iron losses is modeled, but also the influence of different magnetizability is taken into account. The material that is currently in use of the machines production (M400-50A) is compared to two different materials. The steel grade M470-50HP reaches higher maximum values of the magnetic flux density and therefore higher magnetic polarization. This increase of polarization is most likely caused by a higher iron (Fe) content and lower contents of silicon (Si). As a result, the electrical steel conductivity is higher, i.e., higher k_{cl} (see Table I). This high conductivity leads to higher Foucault eddy current losses compared to the other materials. Since the material has a higher magnetizability, less current is necessary at high torque, i.e., high flux operating points. Therefore at high torque operating points, less power losses are dissipated. The maximal loss advantage of M470-50HP is 239 W (ca. 5%) at maximum torque and zero speed (see Fig. 20). At high speeds, i.e., field weakening operation, the advantage of the higher maximum magnetizability has little to none effect. Hence, in high speed operating points (see Fig. 20), the loss behavior of M400-50A is superior with a maximum advantage of 729 W (ca. 15%).

This characteristic behavior of M470-50HP (higher losses at higher speeds and lower losses at high flux operating points compared to M400-50A) is similar to the influence of the air gap length δ. When reducing δ, the coupling of the magnetic circuit is increased and higher magnetic flux (density) values can be achieved with the same magnetization current. However, field harmonics also increase, and, as a result, the acoustic behavior of the machine could be adversely influenced. Thus at high speed operation, higher losses are dissipated. Here, we decrease the air gap from $\delta = 0.5$ to 0.4 mm to find the influence of this effect. Fig. 21 shows the modeled loss difference using M400-50A with $\delta = 0.4$ mm compared to M470-50HP with $\delta = 0.5$ mm. This adapted air gap decreases the loss difference between the two materials. The maximum advantage of M470-50HP of 239 W is reduced to 141 W. At maximum speed, the advantage of M400-50A of 729 W is conversed into a disadvantage of 208 W. These results show, which when designing IMs, the choice of electric steel grade gives a degree of freedom, which could interfere with other design variables, such as the length of air gap.

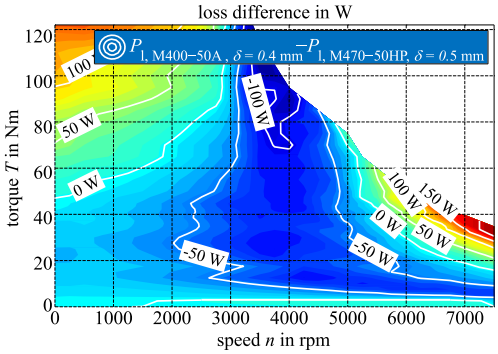

Fig. 21. Simulated difference of the machine power losses when using the two electrical steel grades M400-50A (with reduced air gap of $\delta = 0.4$ mm) and M470-50HP ($\delta = 0.5$ mm).

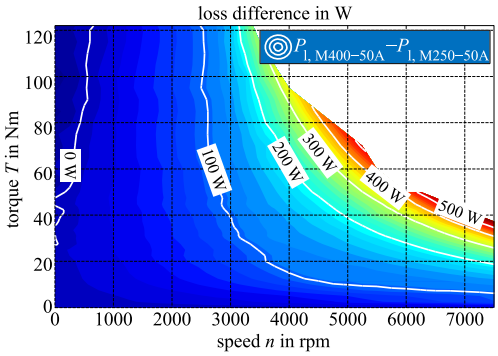

Fig. 22. Simulated difference of the machine power losses when using the two electrical steel grades M400-50A and M250-50A.

For series produced machines, the electric steel laminations are mostly dissected by stamping. Therefore, the number of stampings should be small to minimize manufacturing costs. In contrast to the aim of thick laminations (small manufacturing costs), thinner laminations (smaller d) lead to a decrease of Foucault eddy current losses (3) and (7).

Hence, we compare the possible loss decrease when using electric steel laminations of the same thickness ($d = 0.5$ mm) as well as using thinner laminations with $d = 0.35$ mm. A material with very low losses with $d = 0.5$ mm is M250-50A. M330-35HP has lower losses and is thinner ($d = 0.35$ mm). M250-50A is chosen for the comparison to the status quo (M400-50A). M250-50A and M330-35HP are compared to analyze the influence of material thickness.

Fig. 22 shows the modeled loss difference when using M400-50A to M250-50A. At zero speed and high torque, M400-50A has a slight maximal advantage in losses of 32 W due to slightly better magnetizability. As expected, the steel grade M250-50A leads to less losses at high speeds. The maximum advantage at the maximum speed is 583 W.

Comparing M250-50A to M330-35HP in terms of losses (see Fig. 23) results in smaller differences. The maximum advantage of M250-50A is 14 W at medium speeds (2000 r/min), whereas M330-35HP has less losses at high speeds with a maximum difference of 227 W. Overall, M330-35HP leads to lower losses, although having higher nominal losses at 1.5 T and 50 Hz (sinusoidal flux density waveform).

For the given machine design with a maximum synchronous frequency of 282 Hz, this loss advantage of M330-35HP is rather

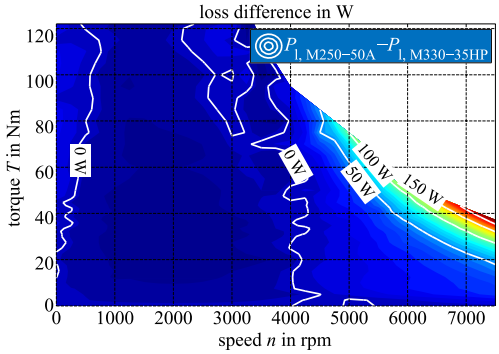

Fig. 23. Simulated difference of the machine power losses when using the two electrical steel grades M250-50A and M330-35HP.

small. Hence, the use of thinner laminations for the studied machine design is most likely not economical.

However, the choice of a lower loss material (e.g., M250-50A) can increase the machines performance without significantly increasing the manufacturing costs of the machine.

IV. Conclusion

This paper presented an in-depth study of the global operating point dependent losses of IMs. The losses of a squirrel cage IM operated as traction drive were modeled using a transient iron loss formulation in the postprocessing of a transient FE simulation at a single synchronous frequency. Since the iron losses are highly dependent on the spatial and temporal distortion of the magnetic flux density, the FE model allows considering these local effects, which significantly contribute the overall losses. In commonly used loss formulations for electric machines, these additional losses are taken into account mostly by building factors. Application of local transient loss calculation to transient two-dimensional FE solutions inherently incorporates these machine- and operation-dependent losses.

From the FE simulation, the Ohmic losses in the stator and rotor were calculated at this single synchronous frequency. From the Ohmic losses and the stator flux linkage from the simulation, the operating points in terms of torque and speed were calculated. These operating points were calculated to yield the lowest Ohmic losses for each point of operation. The limitation of the stator flux linkage due to field weakening operation was regarded.

A scheme to scale the iron losses from one synchronous frequency to the operating frequency in every operating point of the machine was studied and used. Iron loss measurements of the machines core material were conducted using a ring core sample of this material. Iron loss parameters for the iron loss simulation of the machine were extracted from those ring core measurements. The measured friction losses of the machine were added to the modeled losses. A low deviation between the measured and simulated sum of losses was achieved. This loss modeling approach enables for precise machine loss modeling for highly utilized IMs.

The precise modeling of the machines losses from FE simulations and ring core measurements enables to precisely predict the influence of changes in the machines' design. In this paper, particular attention was paid to the effect of different electrical steel grades tailored either to low losses or to preferable

magnetizability, by using the operating point resolved loss calculation approach. The effect of different electrical steel grades and the dimension of the air gap on motor efficiency were investigated. Grades with preferable magnetization behavior result in a good compromise between high torque production and low losses. A higher torque density that can be achieved enables a lighter and smaller machine design as well as design modifications, i.e., variation of the air gap. Furthermore, it was shown that grades with smaller thickness to reduce macroscopic eddy currents do not lead automatically to improved properties for the aimed operating conditions in comparison to thicker grades with increased silicon content. A tradeoff tailored to the individual machine is needed that is not possible based on standardized material data. The proposed transient approach allows studying the influence of the number of poles, diameters, length, and many other design factors on motor efficiency along the torque–speed map.

References

[1] F. Abrahamsen, F. Blaabjerg, J. K. Pedersen, and P. B. Thoegersen, "Efficiency-optimized control of medium-size induction motor drives," *IEEE Trans. Ind. Appl.*, vol. 37, no. 6, pp. 1761–1767, Nov./Dec. 2001.

[2] A. A. Cabezas Rebolledo and M. A. Valenzuela, "Expected savings using loss-minimizing flux on IM drives–Part I: Optimum flux and power savings for minimum losses," *IEEE Trans. Ind. Appl.*, vol. 51, no. 2, pp. 1408–1416, Mar./Apr. 2015.

[3] S. Lim and K. Nam, "Loss-minimising control scheme for induction motors," *Proc. Inst. Elect. Eng.–Elect. Power Appl.*, vol. 151, no. 4, pp. 385–397, Jul. 2004.

[4] G. O. Garcia, J. C. Mendes Luis, R. M. Stephan, and E. H. Watanabe, "An efficient controller for an adjustable speed induction motor drive," *IEEE Trans. Ind. Electron.*, vol. 41, no. 5, pp. 533–539, Oct. 1994.

[5] Q. Zengcai, M. Ranta, M. Hinkkanen, and J. Luomi, "Loss-minimizing flux level control of induction motor drives," in *Proc. IEEE Int. Elect. Mach. Drives Conf.*, May 2011, pp. 1585–1590.

[6] S. A. Odhano, R. Bojoi, A. Boglietti, S. G. Rosu, and G. Griva, "Maximum efficiency per torque direct flux vector control of induction motor drives," *IEEE Trans. Ind. Appl.*, vol. 51, no. 6, pp. 4415–4424, Nov./Dec. 2015.

[7] R. Wrobel, P. H. Mellor, M. Popescu, and D. A. Staton, "Power loss analysis in thermal design of permanent-magnet machines—A review," *IEEE Trans. Ind. Appl.*, vol. 52, no. 2, pp. 1359–1368, Mar./Apr. 2016.

[8] S. Sridharan and P. T. Krein, "Induction motor drive design for traction application based on drive-cycle energy minimization," in *Proc. IEEE 29th Annu. Appl. Power Electron. Conf. Expo.*, Mar. 2014, pp. 1517–1521.

[9] T. Windisch and W. Hofmann, "Loss minimizing and saturation dependent control of induction machines in vehicle applications," in *Proc. 41st Annu. Conf. IEEE Ind. Electron. Soc.*, Nov. 2015, pp. 001530–001535.

[10] A. Boglietti, A. Cavagnino, and M. Lazzari, "Computational algorithms for induction-motor equivalent circuit parameter determination—Part I: Resistances and leakage reactances," *IEEE Trans. Ind. Electron.*, vol. 58, no. 9, pp. 3723–3733, Sep. 2011.

[11] A. Boglietti, A. Cavagnino, and M. Lazzari, "Computational algorithms for induction motor equivalent circuit parameter determination—Part II: Skin effect and magnetizing characteristics," *IEEE Trans. Ind. Electron.*, vol. 58, no. 9, pp. 3734–3740, Sep. 2011.

[12] D. Dorrell, M. Popescu, L. Evans, D. Staton, and A. Knight, "Modern electrical machine analysis and design techniques applied to hybrid vehicle drive machines," in *Proc. IEEE Int. Symp. Ind. Electron.*, Jul. 2010, pp. 3728–3733.

[13] D. Kowal, P. Sergeant, L. Dupre, and H. Karmaker, "Comparison of frequency and time-domain iron and magnet loss modeling including PWM harmonics in a PMSG for a wind energy application," *IEEE Trans. Energy Convers.*, vol. 30, no. 2, pp. 476–486, Jun. 2015.

[14] Z. Gmyrek, A. Boglietti, and A. Cavagnino, "Estimation of iron losses in induction motors: Calculation method, results, and analysis," *IEEE Trans. Ind. Electron.*, vol. 57, no. 1, pp. 161–171, Jan. 2010.

[15] D. Lin, P. Zhou, W. N. Fu, Z. Badics, and Z. J. Cendes, "A dynamic core loss model for soft ferromagnetic and power ferrite materials in transient finite element analysis," *IEEE Trans. Magn.*, vol. 40, no. 2, pp. 1318–1321, Mar. 2004.

[16] S. Zhu, M. Cheng, J. Dong, and J. Du, "Core loss analysis and calculation of stator permanent-magnet machine considering DC-biased magnetic induction," *IEEE Trans. Ind. Electron.*, vol. 61, no. 10, pp. 5203–5212, Oct. 2014.

[17] A. Belahcen and A. Arkkio, "Comprehensive dynamic loss model of electrical steel applied to FE simulation of electrical machines," *IEEE Trans. Magn.*, vol. 44, no. 6, pp. 886–889, Jun. 2008.

[18] P. Rasilo, E. Dlala, K. Fonteyn, J. Pippuri, A. Belahcen, and A. Arkkio, "Model of laminated ferromagnetic cores for loss prediction in electrical machines," *IET Elect. Power Appl.*, vol. 5, no. 7, pp. 580–588, Aug. 2011.

[19] M. Hafner, F. Henrotte, M. Herranz Gracia, and K. Hameyer, "An energy-based harmonic constitutive law for magnetic cores with hysteresis," *IEEE Trans. Magn.*, vol. 44, no. 6, pp. 922–925, Jun. 2008.

[20] E. Dlala, O. Bottauscio, M. Chiampi, M. Zucca, A. Belahcen, and A. Arkkio, "Numerical investigation of the effects of loading and slot harmonics on the core losses of induction machines," *IEEE Trans. Magn.*, vol. 48, no. 2, pp. 1063–1066, Feb. 2012.

[21] J. Lammeraner and M. Stafl, *Eddy Currents*. London, U.K.: Iliffe Books, 1966.

[22] C. Carstensen, "Eddy currents in windings of switched reluctance machines," Ph.D. dissertation, Inst. Power Electron. Elect. Drives (ISEA), RWTH Aachen Univ., Aachen, Germany, 2008.

Georg Von Pfingsten received the Bachelor's and Master's degrees in electrical engineering from RWTH Aachen University, Aachen, Germany, in October 2010 and November 2012, respectively.

Since December 2012, he has been a Research Associate in the Institute of Electrical Machines, RWTH Aachen University. His research interests include induction machine modeling, optimization of induction machines, soft magnetic material modeling, and iron loss calculation in macroscopic scale.

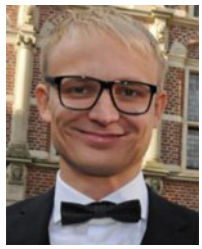

Simon Steentjes received the Diploma degree in electrical engineering from RWTH Aachen University, Aachen, Germany, in November 2011.

Since December 2011, he has been a Research Associate in the Institute of Electrical Machines, RWTH Aachen University. His research interests include hard- and soft-magnetic material modeling on the micro- and macroscopic scales, iron loss calculation, effects of material processing, magnetic forces, and mathematical methods.

Kay Hameyer (M'96–SM'99) received the M.Sc. degree in electrical engineering from the University of Hannover, Hannover, Germany, in 1986, and the Ph.D. degree from the University of Technology Berlin, Berlin, Germany, in 1992, for work on permanent-magnet excited machines.

After his university studies, he worked with Robert Bosch GmbH, Stuttgart, Germany, as a Design Engineer for permanent-magnet servo motors. From 1988 to 1993, he was a Member of Staff at the University of Technology Berlin. From 1996 to 2004, he was a Full Professor of Numerical Field Computations and Electrical Machines, Katholieke Universiteit Leuven (KU Leuven), Leuven, Belgium. Since 2004, he has been a Full Professor and the Director of the Institute of Electrical Machines (IEM), RWTH Aachen University, Aachen, Germany. His research interests include all aspects of the design, control, and manufacturing of electrical machines and the associated numerical simulation. The characterization and modeling of hard- and soft-magnetic materials is another focus of his work. He has authored/coauthored more than 250 journal publications, more than 500 international conference publications, and four books. His research interests include numerical field computation and optimization, and the design and control of electrical machines, in particular, permanent-magnet excited machines and induction machines.

Prof. Hameyer became a Member of the German VDE in 1992 and a Fellow of the Institution of Engineering and Technology, U.K., in 2002.